PHYSICAL REVIEW RESEARCH **4**, 023220 (2022)

# Hidden spatiotemporal sequence in transition to shear band in amorphous solids

Zeng-Yu Yang,[1,2] Yun-Jiang Wang,[1,2] and Lan-Hong Dai[1,2,3,*]
[1] *State Key Laboratory of Nonlinear Mechanics, Institute of Mechanics, Chinese Academy of Sciences, Beijing 100190, China*
[2] *School of Engineering Science, University of Chinese Academy of Sciences, Beijing 100049, China*
[3] *School of Future Technology, University of Chinese Academy of Sciences, Beijing 100049, China*

(Received 11 January 2022; accepted 31 May 2022; published 16 June 2022)

Localization of plastic flow into a narrow shear band is a fundamental and ubiquitous nonequilibrium phenomenon in amorphous solids. Because of the intrinsic entangling of three types of elementary local atomic motion—shear, dilatation, and rotation—the precise physical process of shear band emergence is still an enigma. Here, to unveil this mystery, we formulate a theoretical protocol covering both affine and nonaffine components of deformation, to decode these three highly entangled local atomic-scale events. In contrast to the broad concept of the shear transformation zone, the plastic behavior can be demonstrated comprehensively as the operative manipulation of more exact shear-dominated zones, dilatation-dominated zones, and rotation-dominated zones. Their spatiotemporal evolution exhibits a transition from synchronous motion to separate distribution at the onset of the shear band. The hidden mechanism is then revealed with the help of extreme value theory and percolation analysis. Numerical evidence from extreme value theory indicates that dilatation is the dominant mode at the embryonic stage of the initial plastic units, as evidenced through the larger degree of dilatation localization compared with shear and rotation. The percolation analysis points towards the critical power-law scaling nature at the transition from stochastic activation to percolation of plastic regions. Then the comprehensive picture underlying shear banding emergence is uncovered. Firstly, dilatation triggers initial shear and rotation in soft regions, leading to the embryos of the initial flow units, which are followed by the secondary activation of rotation in neighboring hard material, thus causing an alternating distribution of rotation and shear-dilatation regions. Such rotation activation contributes to further perturbation in these regions and ultimately leads to percolation transition and shear band formation. Our findings also reinforce that the discussion of plastic behavior in disordered materials must take into account both affine and nonaffine component deformation.

DOI: 10.1103/PhysRevResearch.4.023220

## I. INTRODUCTION

Transition from smooth and homogeneous plastic flow to unstable and inhomogeneous flow in the form of a thin, highly localized shear band is a ubiquitous and fundamental nonequilibrium phenomenon in condensed matter ranging from metals to polymers, glasses, colloids, granular media, etc. [1–10]. For metallic glasses, the shear band is their dominant deformation mode at room temperature, which can induce catastrophic fracture with very limited ductility, impeding further engineering applications [1,11–15]. Therefore it is extremely important to explore the physical origin of the shear band in metallic glasses. However, in contrast to their crystalline counterparts, whose plastic flow is given by well-defined topological defects in the periodic lattice such as dislocations, plastic deformation mechanisms of metallic glasses are less well understood due to their inherent structural disorder [16–19]. To date, numerous theoretical models have been proposed to describe local flow events in metallic glasses, such as the free-volume model [11,20,21], shear transformation zone (STZ) [22–24], cooperative shear model [25], flow units [26,27], soft spot [28], and tension transformation zone (TTZ) [29,30], among which the shear transformation zone, involving local rearrangement of a small cluster of atoms, is generally accepted as the elementary process of plastic deformation in metallic glasses [31,32]. In this connection, considerable experimental [33–35] and theoretical attempts [36–39] have been made to find the bridge between the STZ's motion and shear banding emergence. Later simulations indicate that the continued propagation of shear strain occurs by a process of self-assembly: The operation of one STZ creates a localized distortion of the surrounding material and triggers the autocatalytic formation of large planar bands of STZs, causing shear band formation [40–42]. This is so far the most widely accepted scenario of shear banding.

In spite of this, further experimental and simulated evidence collected later on revealed the density variation (or free-volume annihilation and creation process) [34,43–45] as well as vortexlike motion [46–48] in shear banding regions, supporting the general consensus that shear is not necessarily the only deformation mode that accommodates local

---

[*] lhdai@lnm.imech.ac.cn

atomic rearrangement. Actually, shear, dilatation, and rotation are all intrinsic natures of local excitations in metallic glasses, which cannot be fully explained via the classical STZ model. It is the inherent coupling of these deformation events that hinders establishment of an intuitive picture of shear banding emergence in metallic glasses. In this connection, Şopu *et al.* [48] recently proposed the STZ-vortex two-unit model to address the issue of sequential activation of STZs along the direction of the shear band. The STZ-vortex model proposes the mechanism of STZ coalescence with a critical role of rotation events as a catalyst, which mediates distortion between two adjacent STZs [48]. Despite its notable progress in providing an atomistic description of shear banding, the STZ-vortex model has not totally decoded the entangled atomic motions hidden in the nonaffine deformation section. In Ref. [48], the nonaffine displacement [23] was calculated and discussed as a whole; however, it was not decoupled into shear, dilatation, and rotation events. The decoupling method in the STZ-vortex framework is based on the purely affine part of the local displacement field—the local deformation gradient tensor [49]. It should be noted that considering only affine deformation may cause one to miss any meaningful mechanism hidden in the nonaffine components. The latter are also strongly correlated with inhomogeneous plastic deformation in generic disordered materials [23,50,51]. Therefore, to thoroughly unveil the shear banding mechanism at atomic scale, a decoupling framework considering both affine and nonaffine deformation is urgently necessary.

To this end, we propose a theoretical framework that can incorporate both the affine and nonaffine parts of deformation by extensively combining the first- and second-order displacement gradient tensor. As we will later demonstrate via testing simulated $Cu_{50}Zr_{50}$ metallic glass, information from a single affine or nonaffine input can only partially capture the nature of plastic deformation. The addition of a second-order term significantly enhances the capacity of the theoretical model in mapping the real displacement field. On the basis of this powerful framework, we decouple the highly entangled shear, dilatation, and rotation events and thus give the precise identification of these three deformation units. As a step beyond the usual broad concept of STZ percolation, the comprehensive and clear atomic-scale physical process of shear banding is then rationalized via the complicated and obscure interplay between the versatile shear, dilatation, and rotation events. Firstly, shear, dilatation, and rotation are strongly correlated with each other; among them, dilatation plays a dominating role in the embryos of initial plastic events in liquidlike regions. Then, as strain goes on, secondary rotation in adjacent solidlike materials is significantly activated, causing the transition from homogeneous motion to inhomogeneous flow behavior. Such rotation activation contributes to further softening and perturbation in these regions and ultimately leads to the connection of coexisting localized plastic regions characterized as shear band emergence. The connection phenomenon exhibits a percolation transition with power-law scaling nature that is consistent with classical percolation theory. Our findings shed light on the fundamental understanding of shear band formation in metallic glasses and other amorphous materials.

## II. SIMULATION DETAILS

The molecular dynamic simulations were performed using the LAMMPS code [52], with the embedded-atom method (EAM) potential [53] being adopted to describe the atomic interactions for the $Cu_{50}Zr_{50}$ metallic glass. A small sample containing 13 500 atoms was melted from its crystalline phase from 100 to 2100 K and then was equilibrated for 500 ps at 2100 K before being quenched to a glassy state (100 K) at a cooling rate of 0.02 K/ps. A larger model system to be deformed, containing ~660 000 atoms, with dimensions of $37.3 \times 6.2 \times 61.7\ \mathrm{nm}^3$ in the $x$, $y$, and $z$ directions, respectively, was then produced by the replication of the initial glass configuration. The large system was further annealed for 500 ps at 800 K to reduce the artificial boundary effect of multiplication. Periodic boundary conditions were adopted for each direction during the sample preparation process. To ensure that there would be only a single shear band during the deformation, a small notch was created in the rectangular sample to yield a stress concentration on the notch and nucleation of the shear band. Uniaxial loading, with a constant strain rate of $4 \times 10^7\ \mathrm{s}^{-1}$, was employed on the notched sample along the $z$ direction at a low temperature of 100 K. While periodic boundary conditions were imposed along the $y$ and $z$ directions, the free-surface condition was applied in the $x$ direction to enable the occurrence of the shear offset on the free surfaces during the deformation process. The pressure and temperature were controlled using isothermal-isobaric (atom number $N$, pressure $P$, and temperature $T$) ensembles [54] and a Nosé-Hoover thermostat [55,56] for both the sample preparation and uniaxial loading process. The time step of the molecular dynamics was 0.001 ps.

## III. THEORETICAL FRAMEWORK

### A. Mapping the deformation field

Based on the continuum mechanics, the local transformation relation between reference and current configurations during a time interval $\Delta t$ can be described in the form of Taylor expansion:

$$\mathbf{d}^{ij}(t+\Delta t) = \mathbf{F}^i\mathbf{d}^{ij}(t) + \frac{1}{2}\boldsymbol{\eta}^i\mathbf{d}^{ij}(t)^2 + O(\mathbf{d}^{ij}(t)^3). \qquad (1)$$

Here, vectors and tensors are given in bold font. The superscript $i$ and $j$ are used to distinguish different atoms. $\mathbf{d}^{ij}(t)$ is the center-to-center position vector between central atom $i$ and its neighboring $j$th atom. Thus $t = 0$ characterizes the initial configuration before any applied strain. Within the Taylor expansion, the first term, $\mathbf{F}^i\mathbf{d}^{ij}(t)$, denotes the linear relation or affine part of the local displacement field around central atom $i$. $\mathbf{F}^i$ is the deformation gradient tensor with the definition of $\mathbf{F}^i = \mathbf{H}^i + \mathbf{I}$, where the displacement gradient tensor $\mathbf{H}^i$ characterizes the spatial gradient of the displacement field and $\mathbf{I}$ is the identity tensor representing the rigid translation. In terms of this affine part, Shimizu *et al.* [49] identified the local Lagrangian strain tensor $\boldsymbol{\varepsilon}^i = \frac{1}{2}[\mathbf{F}^i(\mathbf{F}^i)^T - \mathbf{I}]$ and proposed a local von Mises strain as $\varepsilon^i_{\mathrm{Mises}} = \sqrt{\varepsilon_{xy}^2 + \varepsilon_{yz}^2 + \varepsilon_{zx}^2 + \frac{(\varepsilon_{xx}-\varepsilon_{yy})^2+(\varepsilon_{xx}-\varepsilon_{zz})^2+(\varepsilon_{zz}-\varepsilon_{yy})^2}{6}}$. Then, the addition of the second- and higher-order terms of Eq. (1),

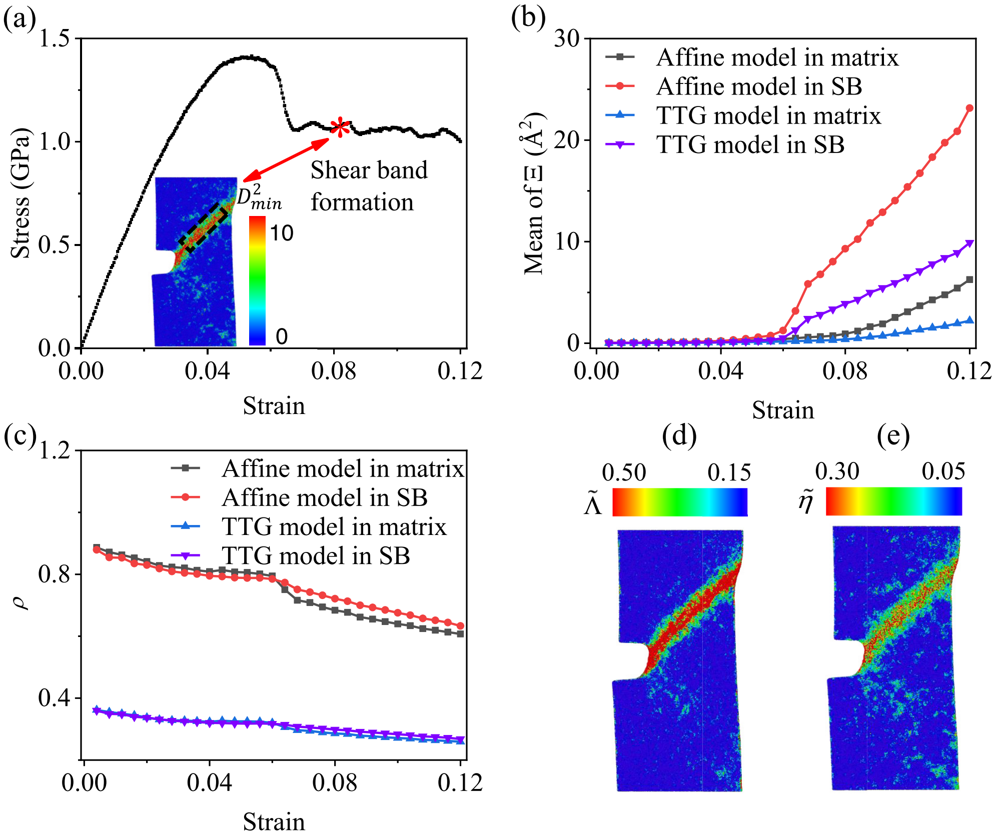

FIG. 1. The power of the TTG model in describing the deformation field of metallic glass. (a) The stress-strain curve and the distribution of $D^2_{\mathrm{min}}$ after yielding, with the dashed box showing the position of the mature shear band. (b) Evolution of residual displacement lost by the affine framework and by the TTG model. (c) Evolution of the relative difference of displacements between the whole deformation field and predictive parts described by the affine model and by the TTG model. (d) Distribution of atomic effective strain at a strain of 0.08. (e) Distribution of atomic effective strain gradient at a strain of 0.08. SB, shear band.

i.e., $\frac{1}{2}\boldsymbol{\eta}^i\mathbf{d}^{ij}(t)^2 + O(\mathbf{d}^{ij}(t)^3)$, constructs the nonaffine part of the displacement field. Here, $O(\mathbf{d}^{ij}(t)^3)$ denotes the higher-order terms, and $\boldsymbol{\eta}^i$ is the second-order displacement gradient tensor, i.e., the strain gradient tensor. To characterize departures from the local affine deformation, Falk and Langer [23] proposed the widely used nonaffine squared displacement $D^2_{\mathrm{min}} = \sum_j [\mathbf{d}^{ij}(t+\Delta t) - \mathbf{F}^i\mathbf{d}^{ij}(t)]^2$.

Both the nonaffine displacement and the local von Mises strain are good measures of deformation and have raised broad interest in and had broad impact on the field of glassy physics [57–60]. However, these two quantities actually characterize distinct parts of deformation in terms of their definitions. On the one hand, the local von Mises strain is the output of the local linear strain field. Thus it depicts the affine part of deformation. On the other hand, $D^2_{\mathrm{min}}$ quantifies departures from the local linear strain field and thus characterizes the nonaffine part. Both of these quantities have achieved great success in mapping deformation of disordered materials [61–63]. However, it is still a challenge to distinguish and characterize the rotation, dilatation, and shear events via these theoretical models, as rotation is mostly related to rigid motion, which is affine, while dilatation as well as shear are dominated by distortion, which is nonaffine. To settle this problem, a further theoretical framework containing both affine and nonaffine deformation is urgently needed, which then drives the birth of our proposed two-term gradient (TTG) model. On the basis of the linear affine formalism, the second term of Eq. (1), which incorporates the strain gradient tensor, is supplemented to recognize the nonaffine part. Thus the displacement field is assumed to vary as

$$\mathbf{d}^{ij}(t+\Delta t) \approx \mathbf{F}^i\mathbf{d}^{ij}(t) + \frac{1}{2}\boldsymbol{\eta}^i\mathbf{d}^{ij}(t)^2. \tag{2}$$

Then, $\mathbf{F}^i$ and $\boldsymbol{\eta}^i$ are calculated by minimizing the mean-square difference between the actual displacement field and that demonstrated by $\mathbf{F}^i$ and $\boldsymbol{\eta}^i$:

$$\Xi^i = \frac{1}{N^i}\sum_j \left[\mathbf{d}^{ij}(t+\Delta t) - \mathbf{F}^i\mathbf{d}^{ij}(t) - \frac{1}{2}\boldsymbol{\eta}^i\mathbf{d}^{ij}(t)^2\right]^2. \tag{3}$$

Here, $N^i$ is the number of neighboring atoms around central atom $i$. The minimum value of $\Xi^i$ is then used to quantify the capacity of our TTG model in mapping the real displacement field.

In this paper, we employ molecular dynamics simulations in a prototypical binary $Cu_{50}Zr_{50}$ glass as a computational microscope to test and demonstrate the TTG model. Figure 1 shows the strong power of the TTG model in describing the real displacement field. It should be noted that for all of the numerical results, the reference configuration [$\mathbf{d}^{ij}(t)$ in the TTG model] is chosen as the initial or undeformed state while the current configuration is then represented by strained states varying with sample strain. Firstly, a typical stress-strain curve is presented in Fig. 1(a), from which it is clear that deformation localization appears at a macroscopic strain of 0.06, while the formation of a mature shear band falls behind at a larger strain (0.08), as marked with an asterisk in the plot. In the inset of Fig. 1(a), the spatial distribution of $D^2_{\mathrm{min}}$ at a strain of 0.08 is shown, and one can visualize the shear banding pattern outlined by the dashed black box. In this sense, atoms in the dashed black box can be characterized as plastic ones which participate in shear banding behavior. Then other atoms belong to the matrix. In Fig. 1(b), we plot the evolution of $\Xi^i$ for atoms in the shear band as well as those taken from the matrix. For comparison, the departure of the displacement field assumed by the affine model from the real one is also presented. It is noted that the affine model is defined as the framework which only uses the first term of Eq. (1), i.e., $\mathbf{F}^i\mathbf{d}^{ij}(t)$, to describe the local displacement field. Here, the behavior of deformation localization can be observed at a strain of 0.06, which meets the stress-strain curve well. More interestingly, the difference between the actual displacement field and the TTG model is much less than that for the affine model. This gives direct evidence for the strong enhancement of mapping power of the TTG model over the linear affine model. It reinforces the importance of incorporating the strain gradient term. To further quantify how much the deformation information is omitted by the TTG model compared with the whole displacement field, we propose the following measure:

$$\rho_{\mathrm{TTG}} = \frac{1}{N}\sum\nolimits_i \frac{\left|\sum_j \left[\mathbf{F}^i\mathbf{d}^{ij}(t) + \frac{1}{2}\boldsymbol{\eta}^i\mathbf{d}^{ij}(t)^2 - \mathbf{d}^{ij}(t)\right]^2 - \sum_j \left[\mathbf{d}^{ij}(t+\Delta t) - \mathbf{d}^{ij}(t)\right]^2\right|}{\sum_j \left[\mathbf{d}^{ij}(t+\Delta t) - \mathbf{d}^{ij}(t)\right]^2}, \tag{4}$$

which is the ratio of the omitted displacements to the actual ones. $N$ is the total number of atoms in the sample. For comparison, a similar definition is used for the affine model:

$$\rho_{\mathrm{affine}} = \frac{1}{N}\sum\nolimits_i \frac{\left|\sum_j \left[\mathbf{F}^i\mathbf{d}^{ij}(t) - \mathbf{d}^{ij}(t)\right]^2 - \sum_j \left[\mathbf{d}^{ij}(t+\Delta t) - \mathbf{d}^{ij}(t)\right]^2\right|}{\sum_j \left[\mathbf{d}^{ij}(t+\Delta t) - \mathbf{d}^{ij}(t)\right]^2}. \tag{5}$$

The ratios $\rho$ for both the affine model and the TTG model as a function of macroscopic strain are shown in Fig. 1(c). They provide direct evidence that the present TTG model with integration of the strain gradient effect leads to much higher mapping capability. The TTG model contains most of the deformation information whether the atom is in the shear band or in the matrix. This implies that deformation in metallic glasses is more related to the nonaffine components, of which the TTG model contains the crucial part—the second-order term. Such success of the TTG model confirms the validity and reliability of our decoupling results and conclusions below.

Before we present the decoupling method in the next section, it is useful to discuss the critical role of the strain gradient in shear banding. Firstly, to quantify plastic deformation at the atomic scale, we introduce the atomic local strain for each atom based on the TTG model. Following the general expression given by Gao *et al.* [64], the microscale strain field incorporating the strain gradient is defined as $\Lambda^i_{mn} = \varepsilon^i_{mn} + \frac{1}{N^i}\sum\limits_j [\frac{1}{2}(\eta^i_{kmn} + \eta^i_{knm})d^{ij}_k(t)]$, where the subscripts $k$, $m$, and $n$ indicate the Cartesian components, e.g., $x$ or $y$ or $z$, and the superscripts $i$ and $j$ are particle indices. Here, $d^{ij}_k(t)$ is the $k$th component of the position of the $j$th neighboring atom relative to center atom $i$ in the reference configuration, and $N^i$ is the number of neighboring atoms around atom $i$. The atomic strain field $\Lambda^i_{mn}$ is thus related to the strain tensor $\varepsilon^i_{mn}$ and strain gradient tensor $\eta^i_{kmn}$. Following the classical plasticity theory, the effective strain in the form of a scalar is then introduced as $\tilde{\Lambda}^i = \sqrt{\frac{2}{3}\Lambda^i_{mn}\Lambda^i_{mn}}$. The spatial distribution of $\tilde{\Lambda}^i$ at a strain of 0.08 is shown in Fig. 1(d); like Falk and Langer's $D^2_{\mathrm{min}}$ [23], $\tilde{\Lambda}^i$ is a good measure of local inelastic deformation. More projected strain fields color-coded by $\tilde{\Lambda}^i$ at various applied strains are shown in Fig. S1 of the Supplemental Material [65]. Then the atomic effective strain gradient in the form of a scalar is introduced as $\tilde{\eta}^i = \sqrt{\frac{1}{4}\eta^i_{kmn}\eta^i_{kmn}}$, which is similar to that of the effective strain [64]. The projected strain gradient field at a strain of 0.08 is plotted in Fig. 1(e). Here, we can find good correspondence between the strain gradient field and the distribution of deformation. More snapshots color-coded by strain gradient are given in Fig. S2 [65]. Local regions with accumulated strain penetrate into each other, and these regions overlap with locations where the strain gradient effect is apparent. This indicates that the strain gradient effect does play an important role in shear banding. To clarify the critical role played by the strain gradient during the shear banding process, the statistics of the effective strain and strain gradient as functions of macroscopic strain are given in Fig. 2. The results are calculated for atoms in the shear band and for atoms in the matrix. They show that the deviation between the shear band and the matrix for the effective strain gradient is earlier than that for the effective strain. This is direct evidence that the strain gradient takes precedence over strain localization and promotes the formation of the shear band. This result is consistent with our previous works [66–68], which demonstrate a self-feedback mechanism in which a high strain gradient, acting as the driving force, will induce inhomogeneous energy dissipation and thus aggravate deformation localization.

### B. Decoupling the entangled shear, dilatation, and rotation events

Next, we explain the proposed method to decouple the entangled shear, dilatation, and rotation events. Here, the index

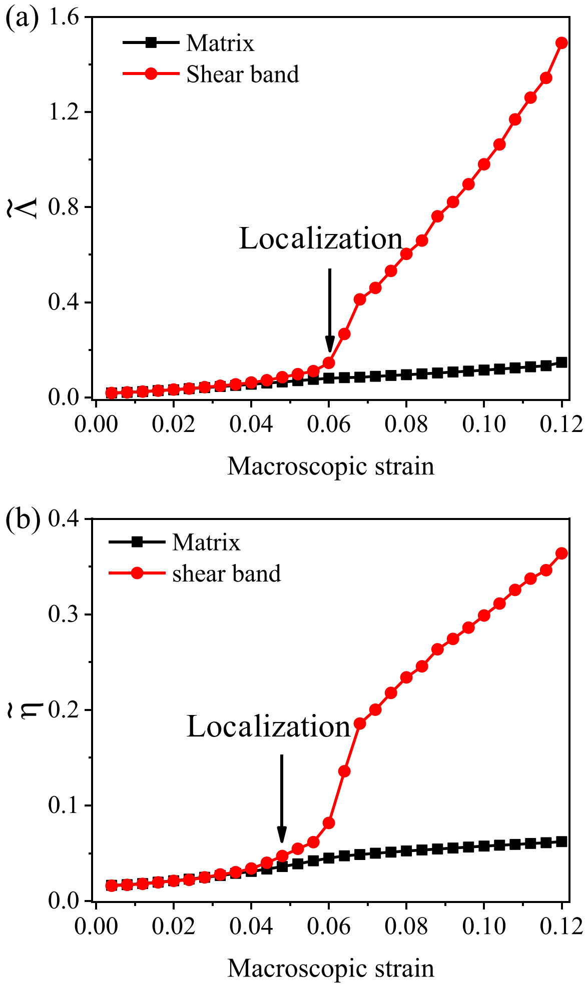

FIG. 2. Evolution of (a) effective atomic strain and (b) effective strain gradient during shear banding. The results are calculated for atoms in the shear band and for atoms in the matrix. The strain gradient effect is apparent in the shear band during deformation. Much of the large strain gradient is located inside of the shear band. The black arrows point out the critical points where the localization of the strain or strain gradient occurs.

notation of tensor analysis is used to demonstrate the details of the decoupling method. In the matter of the affine part, as mentioned above, the deformation gradient tensor $F^i_{mn} = H^i_{mn} + I_{mn}$. As $I_{mn}$ is the identity tensor which represents the rigid translation and contains no effective deformation, we just need to consider the decoupling of the displacement gradient tensor, $H^i_{mn}$, which can be rearranged into three parts, i.e.,

$$H^i_{mn} = \tfrac{1}{2}\left(H^i_{mn} - H^i_{nm}\right) + \left[\tfrac{1}{2}\left(H^i_{mn} + H^i_{nm}\right) - \tfrac{1}{3}\left(H^i_{ll}I_{mn}\right)\right] + \tfrac{1}{3}\left(H^i_{ll}I_{mn}\right), \quad (6)$$

where the terms $\frac{1}{2}(H^i_{mn} - H^i_{nm})$, $[\frac{1}{2}(H^i_{mn} + H^i_{nm}) - \frac{1}{3}(H^i_{ll}I_{mn})]$, and $\frac{1}{3}(H^i_{ll}I_{mn})$ on the right-hand side characterize the rotation, shear, and dilatation components, respectively. All of these are related to affine deformation. That is,

$$\begin{aligned} R^{H,i}_{mn} &= \tfrac{1}{2}\left(H^i_{mn} - H^i_{nm}\right), \\ S^{H,i}_{mn} &= \left[\tfrac{1}{2}\left(H^i_{mn} + H^i_{nm}\right) - \tfrac{1}{3}\left(H^i_{ll}I_{mn}\right)\right], \\ D^{H,i}_{mn} &= \tfrac{1}{3}\left(H^i_{ll}I_{mn}\right). \end{aligned} \quad (7)$$

As for the decoupling method related to the strain gradient tensor, following the notation of Fleck and Hutchinson [69], $D^{\eta,i}_{kmn} = \frac{1}{8}(\delta_{kn}\eta^i_{mll} + \delta_{mn}\eta^i_{kll})$ denotes the hydrostatic, i.e., dilatation part of $\frac{1}{2}\boldsymbol{\eta}^i$. Here, $\delta_{kn}$ is the Kronecker symbol. Then the deviatoric component follows as $\frac{1}{2}\eta'^i_{kmn} = \frac{1}{2}\eta^i_{kmn} - D^{\eta,i}_{kmn}$, of which the fully symmetric tensor $S^{\eta,i}_{kmn} = \frac{1}{6}({\eta'}^i_{kmn} + {\eta'}^i_{mnk} + {\eta'}^i_{nkm})$ is introduced to denote the shear part. Therefore the remaining part, $R^{\eta,i}_{kmn} = \eta'^i_{kmn} - S^{\eta,i}_{kmn}$, can be utilized to specify the rotation related to the strain gradient tensor. Based on the decoupling of the affine and nonaffine deformation, we can introduce the scalar product of these tensors as

$$\begin{aligned} \xi^i_{\mathrm{R}} &= \sqrt{R^{H,i}_{mn}R^{H,i}_{mn}} \cdot \sqrt{R^{\eta,i}_{kmn}R^{\eta,i}_{kmn}}, \\ \xi^i_{\mathrm{D}} &= \sqrt{D^{H,i}_{mn}D^{H,i}_{mn}} \cdot \sqrt{D^{\eta,i}_{kmn}D^{\eta,i}_{kmn}}, \\ \xi^i_{\mathrm{S}} &= \sqrt{S^{H,i}_{mn}S^{H,i}_{mn}} \cdot \sqrt{S^{\eta,i}_{kmn}S^{\eta,i}_{kmn}}, \end{aligned} \quad (8)$$

which are called the rotation transformation factor, dilatation transformation factor, and shear transformation factor, respectively. These factors are used to quantitatively describe the rotation, dilatation, and shear transformation events in the model glass. It should be noted that higher $\xi^i_{\mathrm{R}}$, $\xi^i_{\mathrm{D}}$, and $\xi^i_{\mathrm{S}}$ values indicate a more severe level of corresponding local transformation motion. In Figs. 3(a)–3(c), the representative microscopic motion for all of the rotation, dilatation, and shear events is revealed by virtue of the atomic displacement vectors. As shown in the first column of Fig. 3(a), one can clearly observe the atomic-scale rotation transformation, manifesting as a collective, vortexlike motion. The same analysis on the representative dilatation and shear events is shown in the first column of Figs. 3(b) and 3(c), respectively. The displacement fields denote that the atoms seem to move desultorily compared with those participating in rotation events. If all of these atoms are colored according to their rotation transformation factor $\xi^i_{\mathrm{R}}$, dilatation transformation factor $\xi^i_{\mathrm{D}}$, and shear transformation factor $\xi^i_{\mathrm{S}}$, as shown in the panels of the second to the fourth columns of Figs. 3(a)–3(c), we can carefully observe good spatial correspondence between the distribution of these quantities and the exact locations of rotation, dilatation, and shear events. To be more specific, the bright $\xi^i_{\mathrm{R}}$ regions [colored in red in the second column of Fig. 3(a)] overlap with the vortex core outlined by the displacement field in the first column of Fig. 3(a). The results of dilatation and shear events show a similar correspondence, as evidenced by the consistency between bright $\xi^i_{\mathrm{D}}$ or $\xi^i_{\mathrm{S}}$ fields [colored in red in the third column of Fig. 3(b) and the fourth column of Fig. 3(c), respectively] and atoms with disordered displacement vectors, as shown in the first column of Figs. 3(b) and 3(c), respectively. This correspondence indicates that these three transformation factors, $\xi^i_{\mathrm{R}}$, $\xi^i_{\mathrm{D}}$, and $\xi^i_{\mathrm{S}}$, are

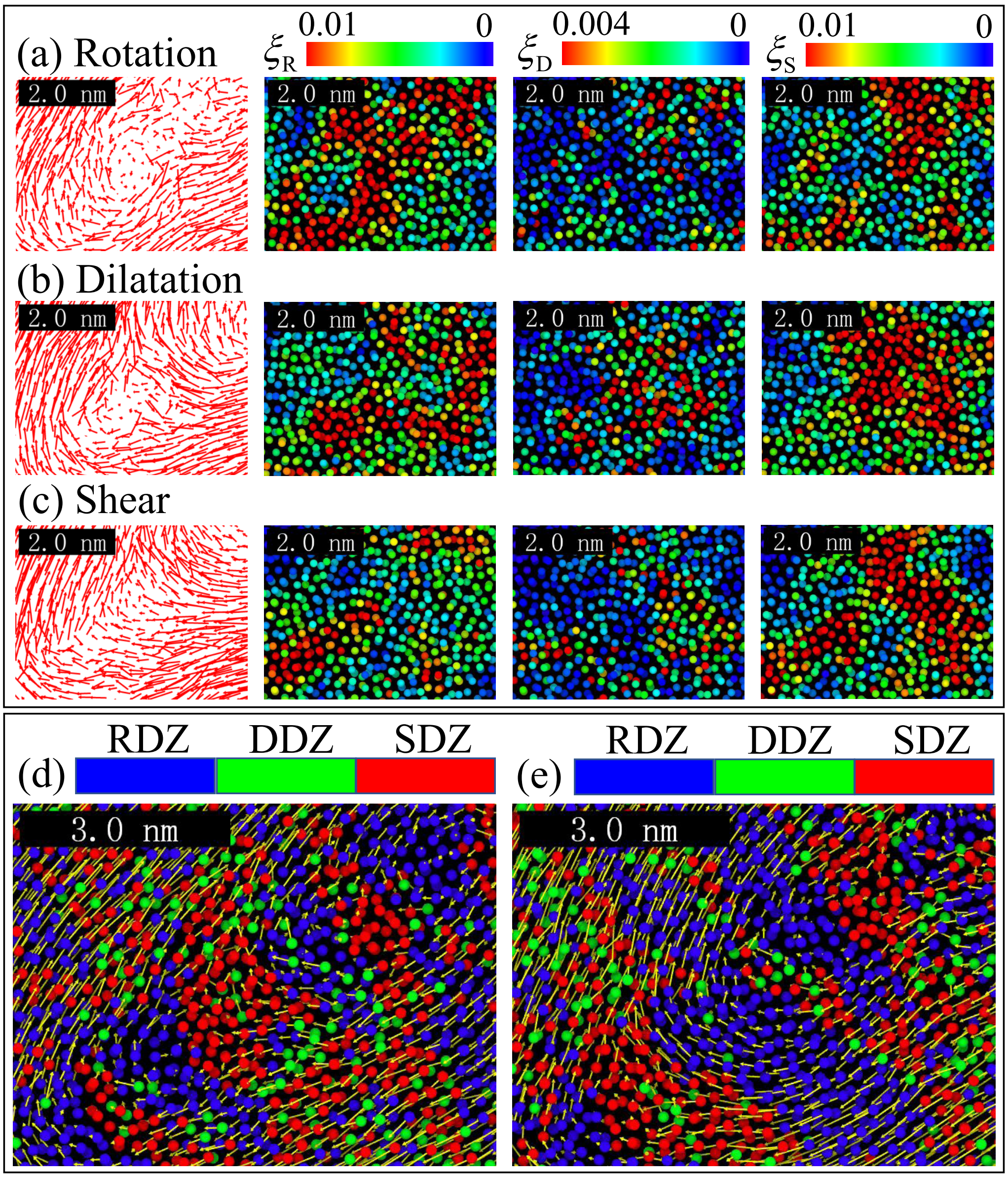

FIG. 3. Representative illustrations of (a) rotation, (b) dilatation, and (c) shear events in the shear band described by the displacement vectors, with magnitudes of $\xi_R$, $\xi_D$, and $\xi_S$ (color-coded), respectively. (d) Representative SDZ and DDZ, where atoms mainly undergo shear and dilatation transformation, as denoted by the red and green atoms, respectively. (e) Representative RDZ, where atoms mainly undergo rotation transformation as denoted by the blue atoms. The yellow arrows represent the displacement vectors, and the atoms are colored according to their RDZ, DDZ, and SDZ labels, respectively. All snapshots are taken with a slice of 5 Å perpendicular to the paper plane.

indeed excellent diagnostics for identifying the local rotation, dilatation, and shear events, respectively.

In order to quantitatively distinguish the relative roles of shear, dilatation, and rotation events at the atomic scale, we further introduce three transformation zones, namely, the rotation-dominated zone (RDZ), dilatation-dominated zone (DDZ), and shear-dominated zone (SDZ). First, the participation fraction of the rotation, dilatation, and shear in the deformation of an atom is defined as

$$\chi_R^i = \frac{\xi_R^i / \xi_R^M}{\sqrt{\left(\xi_R^i / \xi_R^M\right)^2 + \left(\xi_D^i / \xi_D^M\right)^2 + \left(\xi_S^i / \xi_S^M\right)^2}},$$

$$\chi_D^i = \frac{\xi_D^i / \xi_D^M}{\sqrt{\left(\xi_R^i / \xi_R^M\right)^2 + \left(\xi_D^i / \xi_D^M\right)^2 + \left(\xi_S^i / \xi_S^M\right)^2}},$$

$$\chi_S^i = \frac{\xi_S^i / \xi_S^M}{\sqrt{\left(\xi_R^i / \xi_R^M\right)^2 + \left(\xi_D^i / \xi_D^M\right)^2 + \left(\xi_S^i / \xi_S^M\right)^2}}, \quad (9)$$

where $\xi_R^i$ and $\xi_R^M$ denote the value of the rotation transformation factor for atom $i$ and the mean value of atoms residing in the matrix, respectively. Thus we can see that the formula $\xi_R^i/\xi_R^M$ indicates the degree of rotation localization for the $i$th atom. Similar definitions are used for the other two transformation modes, which are given as $\xi_D^i/\xi_D^M$ and $\xi_S^i/\xi_S^M$, respectively. Therefore we can obtain the relative contribution

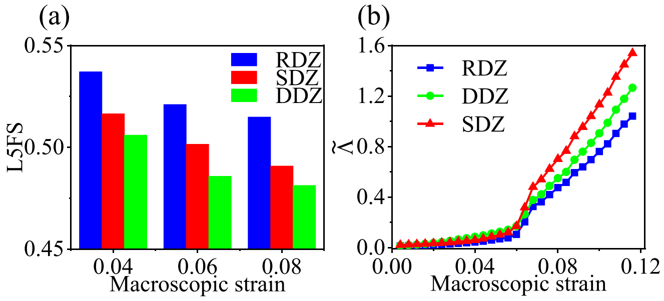

FIG. 4. (a) Comparison of the average magnitudes of the local fivefold symmetry parameter in the RDZ, DDZ, and SDZ at different levels of macroscopic strain. (b) The magnitudes of the atomic strain as a function of macroscopic strain for the atoms evolving into RDZs, DDZs, and SDZs during shear banding. All of the atoms used for the analysis here are taken from the shear band. This figure shows that RDZs are more likely overlapping with solidlike structures and can resist more distortion during deformation.

that each type of event makes to the whole local deformation according to Eq. (9). By using such definitions, we then calculate the participation fraction as $\chi_{\mathrm{R}}$, $\chi_{\mathrm{D}}$, and $\chi_{\mathrm{S}}$ for all of the atoms. The maximum value in the population $\{\chi_{\mathrm{R}}^i, \chi_{\mathrm{D}}^i, \chi_{\mathrm{S}}^i\}$ defines an atomic-scale deformation region to be in either the RDZ, the DDZ, or the SDZ, respectively. This means that a specific deformation event dominates the defined local region of an atom. For example, if $\chi_{\mathrm{R}}^i$ is a maximum in the three parameters, the $i$th atom then belongs to the RDZ. Figures 3(d) and 3(e) show the good correspondence between the labels of RDZ, DDZ, and SDZ and the exact locations of rotation, dilatation, and shear events.

We further investigate the structural origin of the RDZ, DDZ, and SDZ by using the average degree of the local fivefold symmetry parameter (L5FS) [57,70,71]. Here, L5FS is defined on the basis of the widely used Voronoi index, which has the form $\langle n_3, n_4, n_5, n_6, \ldots, n_i, \ldots\rangle$, where $n_i$ denotes the number of $i$-edge polygons. In this connection, L5FS is defined as the fraction of pentagons in each polyhedron, i.e., $\mathrm{L5FS} = n_5/\sum_i n_i$. Figure 4(a) shows the average magnitudes of the L5FS in the RDZ, DDZ, and SDZ at different levels of deformation. It shows that the highest L5FS level appears in the RDZ, compared with those in the DDZ and SDZ. This indicates that rotation events are best correlated with the solidlike regions, which are generally more resistant to deformation. This observation is further verified by the evolution of the effective strain $\tilde{\Lambda}$ residing in the RDZ, DDZ, and SDZ, as shown in Fig. 4(b). It is seen that atoms in SDZs and DDZs are prone to undergo plastic deformation while atoms in RDZs always experience the lowest level of local strain and thus can resist more distortions.

To elaborate more on the concepts of the SDZ, DDZ, and RDZ, we provide a statistical analysis of their size distributions. By using Eq. (9), each atom is labeled as SDZ, DDZ, or RDZ. For a local region with cutoff radius $r$, the ratio $\alpha(r) = (\text{number of RDZ atoms})/(\text{number of total atoms})$ is calculated. The involved atoms in a RDZ can thus be captured by gradually increasing the cutoff radius. Once $\alpha(r) < 0.8$, the cutoff and the participating atoms are recorded. Here, the threshold value 0.8 is used to make sure that rotation indeed dominates the exact local region. Similar definitions are used to measure the cluster size of the DDZ and the SDZ. The results are shown in Fig. 5, where the cumulative frequency as well as frequency are plotted as a function of the number of participating atoms and cluster volume. All the size distributions exhibit an exponential-decay-like distribution, with a large fraction of the clusters being clusters of tens of atoms. According to the result shown by the cumulative frequency, however, there are somewhat local events containing several hundred atoms. This observation is consistent with the widely accepted analysis of the size of the STZ, which attributes to the STZ sizes of between a few and approximately several hundred atoms [22,62,72,73]. This indicates that the SDZ, DDZ, and RDZ are comparable in size to the well-known concept of the STZ.

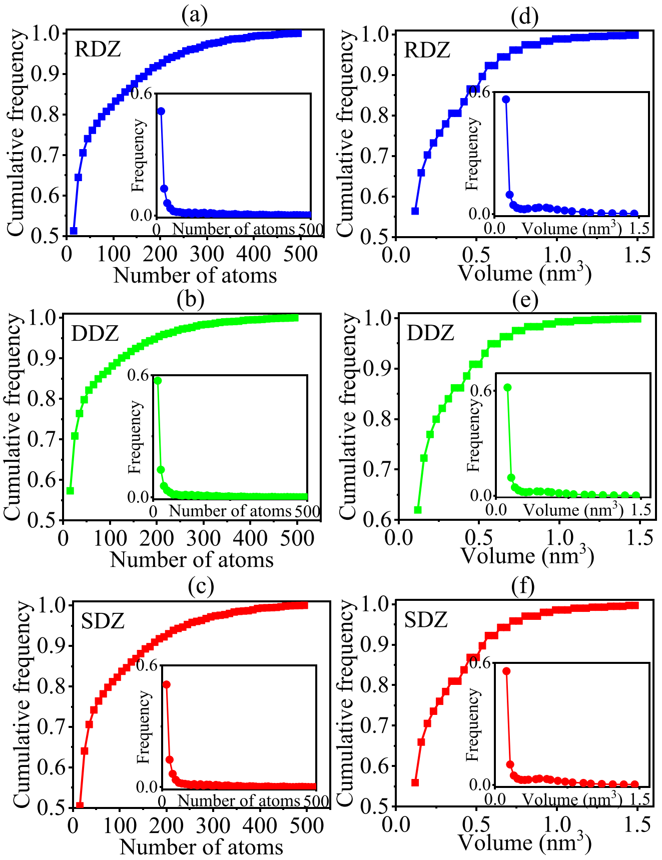

FIG. 5. The size distribution of the RDZs, DDZs and SDZs. (a), (b), and (c) Statistical results for the number of atoms involved in the specific RDZ, DDZ, and SDZ event, respectively. (d), (e), and (f) Statistical results for the volume of clusters of the RDZ, DDZ, and SDZ, respectively. In each panel, the main figure denotes the cumulative frequency, while the inset shows the frequency as a function of cluster size.

## IV. RESULTS AND DISCUSSION

### A. Atomistic scale pattern of shear banding

Having identified the basic deformation units as the RDZ, DDZ, and SDZ, it is now possible to discuss the formation process of the shear band from the perspective of the spatiotemporal evolution of these events. A close inspection of

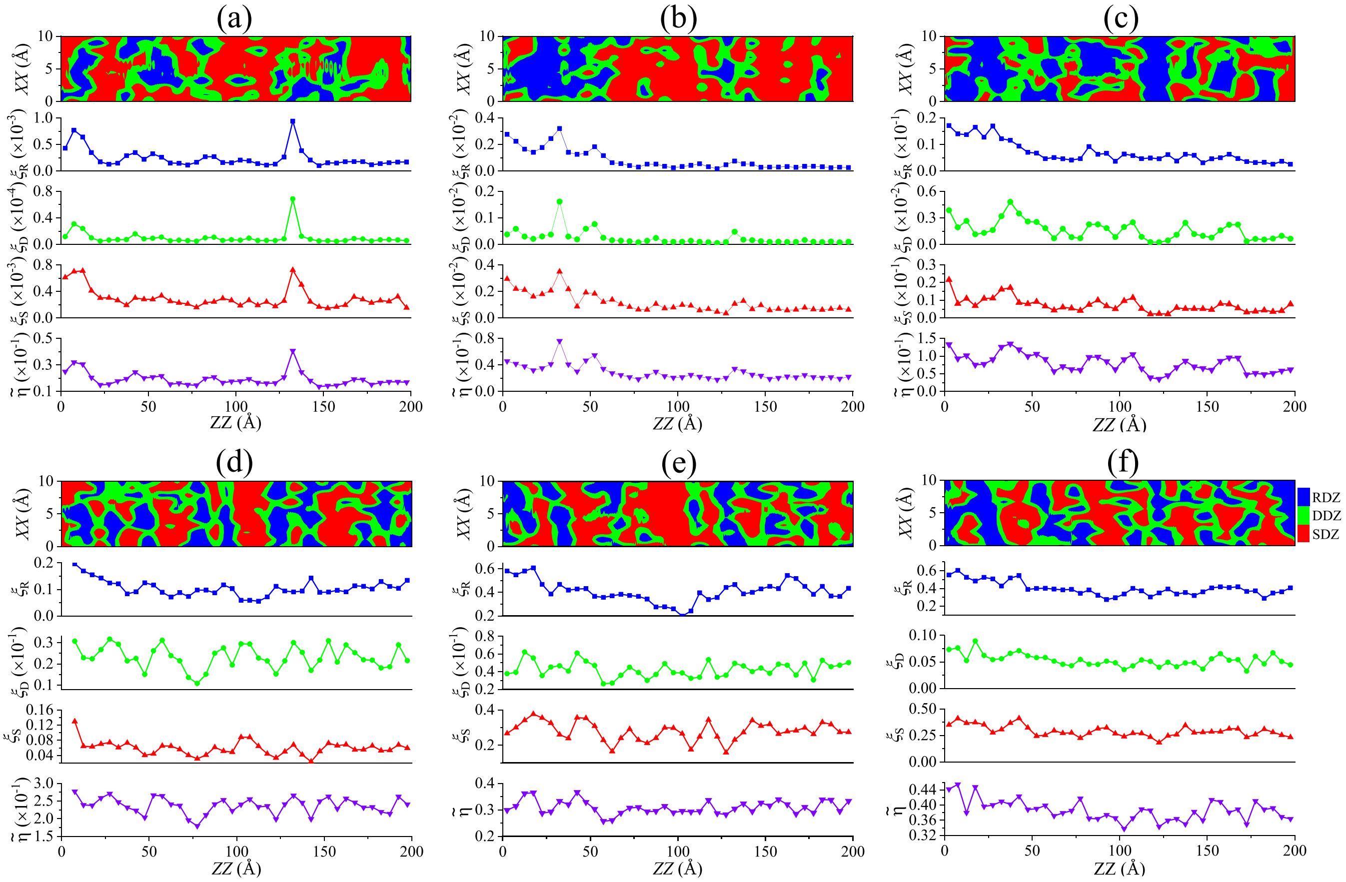

FIG. 6. Spatial and temporal evolution of the RDZ, DDZ, and SDZ, and the corresponding fluctuation of $\xi_R$, $\xi_D$, $\xi_S$, and $\tilde{\eta}$ along the shear band direction. The snapshots are shown at different strain magnitudes of (a) 0.02, (b) 0.04, (c) 0.06, (d) 0.07, (e) 0.08, and (f) 0.10. A mature shear band forms at a strain of 0.08, as demonstrated in Fig. 1(a). A slice of 5 Å along the $y$ direction is coarse-grained for the plot.

the temporal evolution of the RDZ, DDZ, and SDZ maps during shear banding is given in Fig. 6. Here, we can observe that at the strain levels of 0.02, 0.04, and 0.06 [Figs. 6(a)–6(c)], RDZs, DDZs, and SDZs are distributed homogeneously and diffusely. This indicates the synchronous activation and motion of rotation, dilatation, and shear events at the early stage of deformation before the appearance of strain localization. However, when the strain reaches a value of 0.07 [Fig. 6(d)], at which point a shear band is about to emerge, the synchronous motion is broken down with the RDZs and SDZs-DDZs distributed separately. As the deformation proceeds, the shear band forms in the direction of the maximum shear stress with again the homogenous distribution of RDZs, DDZs, and SDZs as the patterns show in Figs. 6(e) and 6(f). To obtain further quantitative insight into the temporal and spatial evolution of the deformation pattern, we bin and reduce the values of $\xi_R$, $\xi_D$, and $\xi_S$ along the shear band direction at different strain levels, i.e., 0.02 and 0.04 (early deformation stage), 0.06 (just before strain localization), 0.07 (strain localization), 0.08 (mature shear band formation), and 0.1 (steady-state flow), as shown in Figs. 6(a)–6(f), respectively, below the deformation pattern. At the early stage of deformation, these three deformation events are homogeneously distributed, and shear, dilatation, and rotation events overlap with each other in the whole sample. However, one can observe an alternating correspondence between the peaks of $\xi_R$ and valleys of $\xi_D$ and $\xi_S$, at a strain of 0.07, at which point strain localization has already formed. Together, these pieces of evidence verify the existence of a transition from synchronous motion to separate distribution of rotation, shear, and dilatation events. Besides, such a transition occurs before the onset of shear banding. In addition, the fluctuation of effective strain gradient $\tilde{\eta}$ is also plotted in Fig. 6 to detail the evolution of the strain gradient distribution. It shows that the fluctuation of the strain gradient field overlaps with that of $\xi_D$ and $\xi_S$, which implies the accumulation of plastic strain in DDZs and SDZs.

Then, it is necessary to figure out when the transition from synchronous motion to inhomogeneous distribution of shear, dilatation, and rotation events happens and what the physical origin hidden in such atomic motion is. To settle such problems, the correlation coefficient is applied to evaluate the evolution of correlation among $\xi_R$, $\xi_D$, and $\xi_S$ in the shear band as $C = \frac{\langle P_1 P_2\rangle - \langle P_1\rangle\langle P_2\rangle}{\sqrt{\langle P_1^2\rangle - \langle P_1\rangle^2}\sqrt{\langle P_2^2\rangle - \langle P_2\rangle^2}}$. Here, $P_1$ and $P_2$ denote two different parameters which can be replaced by $\xi_R$, $\xi_D$, or $\xi_S$. The calculated correlation functions are shown in Fig. 7(a) as a function of macroscopic strain. The positive magnitude of the correlators for $\xi_R$-$\xi_S$ and $\xi_R$-$\xi_D$ during the early stage of deformation indicates the strong positive correlation between shear-dilatation and rotation. This is consistent with the phenomenon that these three atomic events overlap with each other during the early stage of deformation. The

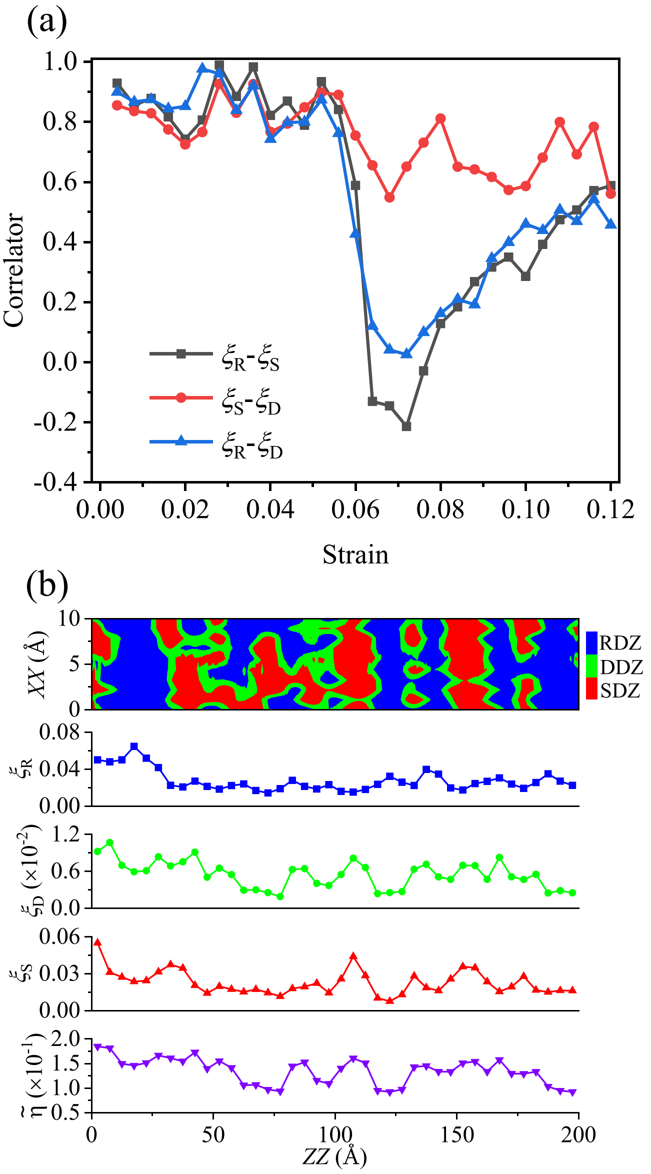

FIG. 7. (a) The evolution of correlation among shear, dilatation, and rotation during deformation. All of the data used for the calculation are taken from the shear band. (b) Spatial distribution of RDZ, DDZ, and SDZ, and their fluctuation along the shear band direction at a strain of 0.064.

abrupt decrease of the correlator of $\xi_R$-$\xi_S$ and $\xi_R$-$\xi_D$ from strain = 0.06 to strain = 0.064 shown in Fig. 7(a) clarifies the synchronization-separation transition with an alternating distribution sequence between shear-dilatation and rotation. Thus it can be concluded here that the separating distribution of shear-dilatation and rotation occurs at a strain of 0.064. To confirm this, the spatial distribution of RDZs, DDZs, and SDZs and the corresponding fluctuations of $\xi_R$, $\xi_D$, $\xi_S$, and $\tilde{\eta}$ along the direction of the shear band at a strain of 0.064 are plotted in Fig. 7(b).

The next task at hand is to figure out what causes the transition from synchronous motion to separate distribution of shear, dilatation, and rotation during such a short period. Colored maps of $\xi_S$ for atoms inside the shear band at strains of 0.06 and 0.064 are plotted in Figs. 8(a) and 8(b), respectively. For a direct comparison, the instant RDZs are superimposed in Figs. 8(a) and 8(b), where white spheres, whose sizes are proportional to the magnitude of $\xi_R$, represent the atoms that have been labeled RDZs. The figure shows that the relative distribution of $\xi_S$ in the snapshot where the strain level is 0.06 is similar to that in the snapshot where the strain level is 0.064 since the locations of regions with relatively high and low values of $\xi_S$ are almost the same between the two snapshots. In contrast, the rotation degree for RDZs adjacent to shear-dilatation zones is strongly enhanced during this short period, thus resulting in the alternating distribution of shear-dilatation and rotation at a strain of 0.064. Actually, the process of enhancing rotation took place earlier, probably at a strain of 0.05, when the $\xi_R$-$\xi_D$ and $\xi_R$-$\xi_S$ correlators begin to attenuate. It is during the short period of 0.06–0.064 that the rotation-increasing behavior becomes obvious. The fact that RDZs are strongly correlated with initial hard clusters indicates that solidlike regions along the shear band direction

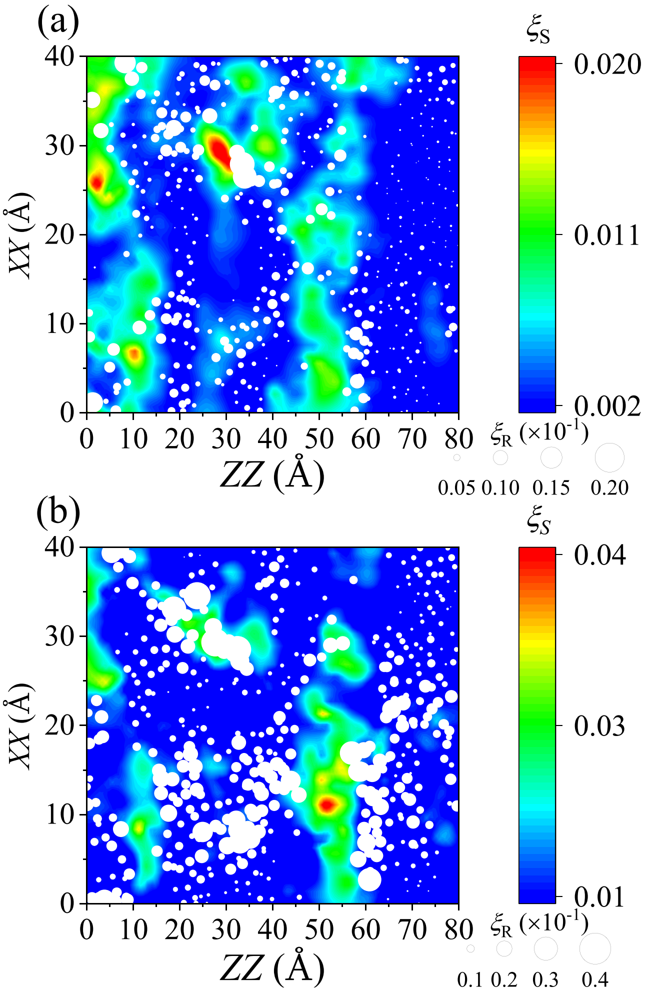

FIG. 8. The rotation degree of the RDZ between two shear-dilatation regions is enhanced during short period from strain = 0.06 to strain = 0.064. The contour maps show the distribution of $\xi_S$ at strains of 0.06 (a) and 0.064 (b). The white spheres superimposed on the contour maps indicate the positions of the atoms that are labeled RDZs. The size of the white spheres denotes the magnitude of $\xi_R$.

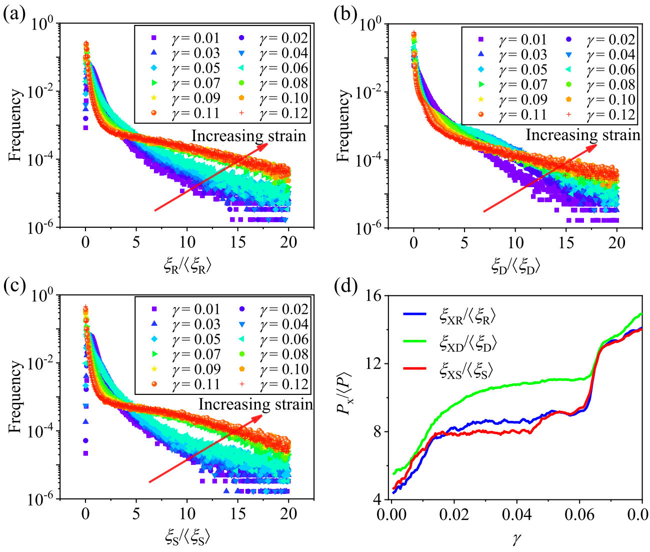

FIG. 9. Extreme value analysis of rotation, dilatation, and shear events in metallic glass. (a)–(c) Statistical distribution of the extreme values normalized by the mean value for rotation (a), dilatation (b), and shear (c) at various applied strains. (d) The evolution of the normalized extreme value, $\xi_{XR}/\langle\xi_R\rangle$, $\xi_{XD}/\langle\xi_D\rangle$, and $\xi_{XS}/\langle\xi_S\rangle$, during the shear banding process.

would undergo a second activation of rotation that is more severe than the first one before softening. Such an enhancement of the rotation event is similar to vortex stretching, which usually contributes to the energy dissipation process [74]. In this sense, this class of severe rotation plays an important role in dissipating energy and further softening in the exact regions. A similar pattern is further given in Fig. S3 [65], in which the spatial distribution of $\xi_R$, $\xi_D$, and $\xi_S$ at strains of 0.06 and 0.064 is plotted. It shows that the rotation degree of regions surrounding shear and dilatation zones is enhanced, while the relative distribution of $\xi_S$ is almost the same as it is at a strain of 0.06. It is more interesting to find the somewhat enhanced dilatation residing in the newly activated RDZs. This is direct evidence of dilatation softening of RDZs which is followed by a percolating process and thus the formation of a shear band. Such a percolating mechanism will be discussed in detail in the following section.

### B. Extreme statistics of initial plastic events

As mentioned above, the picture is clear that the secondary activation of rotation events (here, we refer to the rotation together with shear and dilatation at the early stage as the first activation) and the following softening of RDZs occur at the onset of shear banding. However, the precious identification of initial activation of distorting units via shear, dilatation, and rotation at an earlier stage still remains elusive.

To clarify the respective roles of shear, dilatation, and rotation in this process, we apply the extreme value theory [75–77] to analyze the localization behavior of these three deformation events and how it varies with macroscopic strain. First of all, the transformation factors $\xi_R$, $\xi_D$, and $\xi_S$ are rescaled by their mean values $\langle\xi_R\rangle$, $\langle\xi_R\rangle$, and $\langle\xi_R\rangle$, respectively. Figures 9(a)–9(c) show the probability density distribution of these reduced factors at various applied strains. It shows that the peak probability always stays at ~1 without obvious transitions even for the maximum applied macroscopic strain. The main difference is the much longer tail of the distribution as the strain increases. Such long tails at extreme sites for all of the distributions of $\xi_R/\langle\xi_R\rangle$, $\xi_D/\langle\xi_D\rangle$, and $\xi_S/\langle\xi_S\rangle$ indicate the onset of inhomogeneous flow for rotation, dilatation, and shear units.

To further quantify the evolution of such long-tailing behavior for rotation, dilatation, and shear, we track the extreme sites residing in the long tail. Atoms with the highest 1% value of transformation factors are picked out. The reduced mean value of these atoms ($P_X/\langle P\rangle$, where $P_X$ denotes the extreme values of $P$ and $P$ can be replaced by $\xi_R$ for rotation, $\xi_D$ for dilatation, and $\xi_S$ for shear) is used to measure the degree of heterogeneity for different deformation events. The evolutions of $\xi_{XR}/\langle\xi_R\rangle$, $\xi_{XD}/\langle\xi_D\rangle$, and $\xi_{XS}/\langle\xi_S\rangle$ as functions of macroscopic strain are shown in Fig. 9(d). It shows that the long-tail behavior for all of the rotation, dilatation, and shear events experiences two-step growth before the formation of a mature shear band at a strain of 0.08. One step is at the embryonic stage of deformation characterizing the initial activation of rotation, dilatation, and shear. The other step takes place at the critical time of percolation, which will be discussed in detail in the next section. The long plateaus adjacent to these two abrupt enhancements imply the existence of a cage effect or percolation barrier before shear banding. As $P_X/\langle P\rangle$ is dimensionless, we can compare the degrees of rotation, dilatation, and shear contributing to the whole localization behavior directly. It is interesting to find that dilatation has the most important role compared with rotation and shear at the early stage of deformation. This is direct evidence verifying the dominating role played by dilatation during early deformation. Based on this evidence, the scenario for the initial deformation process emerges: When strain is applied, soft regions in metallic glass mainly undergo the dilatation event and generate free volume, within which atoms are permitted to do further rotation and shear motion, thus causing the activation of initial plastic units. To test whether the stress concentration introduced by the notch would influence the operations of SDZs, DDZs, and RDZs, we conducted an additional tensile test on a glass sample without a notch. The simulation results are shown in Fig. S4 [65]. It shows that the magnitude of stress of the glass without a notch is much higher than that of the notched sample. Besides, the yielding behavior of the sample without a notch takes place later than for the notched one. According to the extreme value analysis shown in Fig. S4(b) [65], dilatation localization also dominates the initial plastic events in the glass sample without a notch. This indicates that the notch will not affect the initial operations of shear, dilatation, and rotation. It is the intrinsic nature of plastic deformation in metallic glasses that dilatation plays a dominating role at the early stage of deformation. However, the stress concentration induced by the notch will influence the nucleation site of the initial activation of dilatation, as evidenced by Fig. S5 [65], where the spatial distribution of the dilatation transformation factor and the mean stress are plotted together. It shows that the nucleation of the initial dilatation events takes place near the notch where stress concentration occurs.

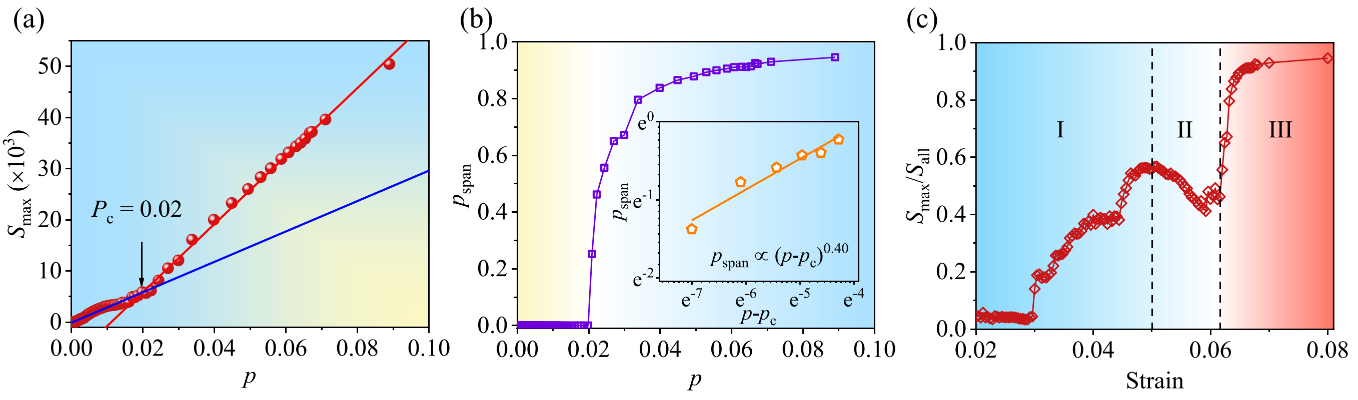

FIG. 10. Percolation analysis in metallic glass. (a) Size of the maximum percolating cluster as a function of $p$. Here, the critical fraction $p_c$ is characterized as 0.02. (b) Variation of percolating probability, $p_{\rm span}$, with $p$. The inset shows a power-law statistic, $p_{\rm span} \propto (p - p_c)^\beta$ with exponent 0.40, which is consistent with the classical scaling behavior in percolation analysis for three dimensions [78]. (c) Time evolution of the percolating factor, $S_{\rm max}/S_{\rm all}$, displaying three characteristic flow steps (regimes I–III) before shear banding formation.

### C. Percolation transition and shear banding emergence

The remaining question is how these coexisting localized plastic regions, dominated by the initial dilatation events, span to large scales in the form of shear bands. To settle this problem, we apply percolation analysis, which usually provides a complementary framework for analyzing the nature of shear banding in metallic glass and other disordered materials [77–80]. Firstly, we define an atom as being plastic or not by setting a threshold of 0.25 for the effective atomic strain $\tilde{\Lambda}$. Snapshots of plastic atoms at various applied strains are shown in Fig. S6 [65], where one can observe a clear transition from stochastic activation to percolation of plastic regions with increasing strain. To quantify and characterize the occurrence of percolation transition, we monitor the fraction of plastic atoms, $p$, as well as the number of plastic atoms residing in the maximum percolating cluster, $S_{\rm max}$. Figure 10(a) plots $S_{\rm max}$ as a function of $p$, which shows that beyond a critical fraction $p_c = 0.02$, tremendous amounts of plastic atoms are covered in the maximum cluster. It is of note that the critical fraction $p_c$ is determined by examination of the discontinuity in the slope of the $S_{\rm max}$-$p$ curve, as pointed out by the intersection of the red and blue lines in Fig. 10(a). This indicates the occurrence of the percolation transition. It should be noted here that $p_c = 0.02$ is smaller than the result of classical percolation analysis for three dimensions [78]. This is because the presence of a notch in the sample used in this paper leads to stress concentration near the notched region, thus bringing the transition forward. Above the percolation threshold, we can figure out the spanning cluster which is exactly the shear band. Here, we compute the probability that a plastic atom belongs to the spanning cluster, namely, $p_{\rm span}$. Then we plot in Fig. 10(b) the evolution of $p_{\rm span}$ as a function of $p$, which shows that $p_{\rm span}$ will dramatically increase when $p$ exceeds the critical point $p_c = 0.02$. Then, it quickly converges to ∼1, indicating that all the plastic atoms are part of such a spanning cluster or shear band. In the inset of Fig. 10(b), we plot the power-law statistics when $p$ approaches $p_c$ from above. Here, it is evident that we observe a power-law scaling behavior $p_{\rm span} \propto (p - p_c)^\beta$ with a critical exponent of 0.4, which is consistent with the classical scaling nature in percolating analysis for three-dimensions [78]. Actually, $\beta = 0.4$ is a universal value only depending on the dimension of the sample. This is direct evidence that the connection of existing localized plastic units, manifesting as shear banding emergence, follows the mechanism of classical percolation transition.

To characterize an accurate physical picture of shear banding emergence, we further investigate the time evolution of the percolating process evaluated by the fraction of the largest percolating cluster in all plastic atoms, $S_{\rm max}/S_{\rm all}$, namely, the percolating factor. Here, $S_{\rm all}$ denotes the number of atoms that have undergone plastic events at an instant in time, while $S_{\rm max}$ characterizes the size of the percolating cluster. Thus the abrupt increase in $S_{\rm max}/S_{\rm all}$ can catch the occurrence of percolating events. Figure 10(c) plots the time evolution of the percolating factor, $S_{\rm max}/S_{\rm all}$, which shows three characteristic regimes before shear banding formation. In regime I, dilatation drives the stochastic activation of liquidlike regions as mentioned above; thus $S_{\rm max}/S_{\rm all}$ increases as strain proceeds, with two-step growth characterizing the local percolating events near the notch region. In regime II, $S_{\rm max}/S_{\rm all}$ decays with the increasing strain. This indicates that the percolating process in the shear band is sluggish while new activation events in the matrix still go on, causing the growth speed of the percolating cluster to be less than that of stochastic activation. The hidden mechanism is that the solidlike clusters near the coexisting activated regions function as obstacles hindering the broadening of plastic events. As mentioned before, these solidlike clusters adjacent to initial plastic regions will be characterized as the secondary activated RDZs with the rotation degree dramatically enhanced during this period, as shown in Fig. 8. This in turn enhances the softening of hard RDZs, which is followed by the percolating transition at the critical point as shown in regime III. Finally, $S_{\rm max}/S_{\rm all}$ converges to ∼1, implying the formation of a mature shear band.

### D. Comprehensive mechanism of the shear band

Having identified the temporal and spatial sequence of the elementary units—dilatation, rotation, and shear—in shear banding, it is now possible to discuss the comprehensive mechanism of shear band formation led by the collective motion of shear, dilatation, and rotation events with the help of the extreme value theory and percolation analysis mentioned above. In this connection, the shear banding process can be separated into four critical steps. In step 1, owing to the disordered structure of metallic glasses, the atoms can exhibit a variety of local environments, causing the inhomogeneous distribution of stable and unstable clusters. Then, as the strain proceeds, dilatation events of soft regions are activated, causing the dilatation localization over the matrix, which is recognized as step 2. The dominating role played by dilatation during the initial activation of plastic events has been verified by extreme value analysis; see Fig. 9. The free volume induced by the dilatation events is enough for the atoms residing in the dilating regions to be able to undergo further shear and rotation motion. In this period, the spatial distributions of dilatation, shear, and rotation are nesting within each other; see Figs. 6(a)–6(c). Such distorting units containing dilatation, shear, and rotation are actually the familiar concept of the STZ. However, decoupling the three entangled events makes the physical process of stochastic activation clearer, where the picture of dilatation pioneering shear and rotation is firstly proposed.

In step 3, the further broadening of plastic deformation in the soft regions is hindered by the surrounding hard clusters, causing the accumulation of a strain gradient in the initial plastic regions. As evidenced by the structural features of RDZs in Fig. 4, atoms in hard clusters mainly undertake rotating motion. As strain goes on, the rotation degree of those solidlike clusters adjacent to initial plastic regions is dramatically enhanced, as shown in Fig. 8. In contrast to the initial activation of rotation events together with shear and dilatation in soft regions, this secondary activation of rotation is stronger and constitutes the concept of RDZ in this paper. Therefore we can visualize the correlation decrease of $\xi_\mathrm{R}$-$\xi_\mathrm{D}$ and $\xi_\mathrm{R}$-$\xi_\mathrm{S}$ and, as a consequence, the transition from synchronous motion to separate distribution of SDZs-DDZs and RDZs during such a short time period; see Figs. 6(d) and 7. Such rotation motion, much like the vortex-stretching process [74,81,82], in turn contributes to the energy cascade process and further aggravates the dilatation of the border of these RDZs. This is verified by Fig. 6, where the boundary of RDZs is entangled with DDZs. This shows the critical role of rotation during the further softening of hard clusters along the direction of shear banding. In the final step, step 4, when the softening of RDZs reaches the limit, which is at the critical point of percolating, the well-activated distorting units will connect with each other, driving the emergence of the shear band in the direction of maximum stress.

## V. CONCLUSION

In summary, we propose a theoretical TTG framework by categorizing the displacement gradient tensor and strain gradient tensor into three parts and thus decouple the entangled shear, dilatation, and rotation events hidden in the deformation of metallic glasses. The proposed TTG model in this paper simultaneously captures the mechanism from both affine and nonaffine perspectives. This combination gives rise to a more comprehensive and more effective description of the cooperative shear, dilatation, and rotation events beyond the conventional, purely affine or nonaffine model. The proposed transformation factors, $\xi_\mathrm{S}$, $\xi_\mathrm{D}$, and $\xi_\mathrm{R}$, can accurately quantify the degree of shear, dilatation, and rotation events, respectively. From the perspective of the participation fraction, SDZs, DDZs, and RDZs are defined to reveal the physical mechanism of shear band formation. At low strain, SDZs, DDZs, and RDZs are strongly coupled with each other, leading to stochastic activation of initial plastic events in soft regions. The extreme value theory results suggest that the predominant process during the activation of initial plastic units is the dilatation of liquidlike spots. This is in good agreement with early theoretical works based on continuum mechanics [1,11,38]. The present work further gives direct atomic evidence that dilatation softening is the root source for the onset of strain localization. It is also found that before the softening of the exact solidlike clusters adjacent to initial plastic regions, the rotation degree in these hard regions will be significantly enhanced, causing the secondary activation of RDZs there. This activation of RDZs is at a dominating level compared with the first one and causes the transition from synchronous activation to inhomogeneous plastic motion which is effectively characterized by the separately distributed SDZs, DDZs, and RDZs. Such severely rotating motion further aggravates the softening of hard regions and contributes to the directional perturbation process as well as ultimate shear band formation. Our percolation analysis yields the critical power-law scaling nature of shear banding, with scaling exponent in analogy with classical percolating theory. It demonstrates how the coexisting localized plastic regions span to large scales in the form of shear banding and confirms the above three-unit atomistic description of the shear banding mechanism.

Therefore we believe that our atomic-scale scenario of shear band emergence may provide a fundamental understanding of the nature of rheological behavior in metallic glass. While this study concentrates on the metallic glass, the TTG model, relying on atomic position alone, can be directly applied to other disordered materials. The incorporation of both affine and nonaffine components of deformation may open up new opportunities to gain deep conceptual understanding not achieved via conventional models.

## ACKNOWLEDGMENTS

This work was supported by the NSFC (Grants No. 11790292 and No. 12072344), the NSFC Basic Science Center Program for Multiscale Problems in Nonlinear Mechanics (Grant No. 11988102), and the opening project of the State Key Laboratory of Explosion Science and Technology, Beijing Institute of Technology (Grant No. KFJJ18-14M). The work was also supported by the Strategic Priority Research Program (Grants No. XDB22040302 and No. XDB22040303), the Key Research Program of Frontier Sciences (Grant No. QYZDJSSWJSC011), and the Youth Innovation Promotion Association of CAS (Grant No. 2017025).

[1] A. Greer, Y. Cheng, and E. Ma, Shear bands in metallic glasses, Mater. Sci. Eng. R **74**, 71 (2013).

[2] C. A. Schuh, T. C. Hufnagel, and U. Ramamurty, Mechanical behavior of amorphous alloys, Acta Mater. **55**, 4067 (2007).

[3] M. L. Falk and J. Langer, Deformation and failure of amorphous, solidlike materials, Annu. Rev. Condens. Matter Phys. **2**, 353 (2011).

[4] C. M. Gourlay and A. K. Dahle, Dilatant shear bands in solidifying metals, Nature (London) **445**, 70 (2007).

[5] P. Schall and M. Van Hecke, Shear bands in matter with granularity, Annu. Rev. Fluid Mech. **42**, 67 (2010).

[6] A. Furukawa and H. Tanaka, Inhomogeneous flow and fracture of glassy materials, Nat. Mater. **8**, 601 (2009).

[7] Y. Bai and B. Dodd, *Adiabatic Shear Localization* (Pergamon, Oxford, 1992).

[8] A. Wisitsorasak and P. G. Wolynes, Dynamical theory of shear bands in structural glasses, Proc. Natl. Acad. Sci. USA **114**, 1287 (2017).

[9] W. H. Wang, Dynamic relaxations and relaxation-property relationships in metallic glasses, Prog. Mater. Sci. **106**, 100561 (2019).

[10] N. Yan, Z. Li, Y. Xu, and M. A. Meyers, Shear localization in metallic materials at high strain rates, Prog. Mater. Sci. **119**, 100755 (2021).

[11] F. Spaepen, A microscopic mechanism for steady state inhomogeneous flow in metallic glasses, Acta Metall. **25**, 407 (1977).

[12] J. S. Langer, Microstructural shear localization in plastic deformation of amorphous solids, Phys. Rev. E **64**, 011504 (2001).

[13] M. L. Manning, E. G. Daub, J. S. Langer, and J. M. Carlson, Rate-dependent shear bands in a shear-transformation-zone model of amorphous solids, Phys. Rev. E **79**, 016110 (2009).

[14] T. Egami, T. Iwashita, and W. Dmowski, Mechanical properties of metallic glasses, Metals (Basel) **3**, 77 (2013).

[15] L. H. Dai, Shear banding in bulk metallic glasses, in *Adiabatic Shear Localization: Frontiers and Advances*, edited by B. Dodd and Y. Bai (Elsevier, Oxford, 2012), 2nd ed., pp. 311–361.

[16] Y. Q. Cheng and E. Ma, Atomic-level structure and structure-property relationship in metallic glasses, Prog. Mater. Sci. **56**, 379 (2011).

[17] Y. Fan, T. Iwashita, and T. Egami, How thermally activated deformation starts in metallic glass, Nat. Commun. **5**, 5083 (2014).

[18] J. C. Ye, J. Lu, C. T. Liu, Q. Wang, and Y. Yang, Atomistic free-volume zones and inelastic deformation of metallic glasses, Nat. Mater. **9**, 619 (2010).

[19] H. Tong and H. Tanaka, Revealing Hidden Structural Order Controlling Both Fast and Slow Glassy Dynamics in Supercooled Liquids, Phys. Rev. X **8**, 011041 (2018).

[20] F. Spaepen, Homogeneous flow of metallic glasses: A free volume perspective, Scr. Mater. **54**, 363 (2006).

[21] Y. Wang, M. Li, and J. Xu, Free volume gradient effect on mechanical properties of metallic glasses, Scr. Mater. **130**, 12 (2017).

[22] A. S. Argon, Plastic deformation in metallic glasses, Acta Metall. **27**, 47 (1979).

[23] M. L. Falk and J. S. Langer, Dynamics of viscoplastic deformation in amorphous solids, Phys. Rev. E **57**, 7192 (1998).

[24] A. Lemaître, Rearrangements and Dilatancy for Sheared Dense Materials, Phys. Rev. Lett. **89**, 195503 (2002).

[25] W. L. Johnson and K. Samwer, A Universal Criterion for Plastic Yielding of Metallic Glasses with a $(T/T_g)^{2/3}$ Temperature Dependence, Phys. Rev. Lett. **95**, 195501 (2005).

[26] Z. Lu, W. Jiao, W. H. Wang, and H. Y. Bai, Flow Unit Perspective on Room Temperature Homogeneous Plastic Deformation in Metallic Glasses, Phys. Rev. Lett. **113**, 045501 (2014).

[27] Z. Wang and W. H. Wang, Flow units as dynamic defects in metallic glassy materials, Natl. Sci. Rev. **6**, 304 (2019).

[28] J. Ding, S. Patinet, M. L. Falk, Y. Cheng, and E. Ma, Soft spots and their structural signature in a metallic glass, Proc. Natl. Acad. Sci. USA **111**, 14052 (2014).

[29] M. Q. Jiang, Z. Ling, J. X. Meng, and L. H. Dai, Energy dissipation in fracture of bulk metallic glasses via inherent competition between local softening and quasi-cleavage, Philos. Mag. **88**, 407 (2008).

[30] X. Huang, Z. Ling, and L. H. Dai, Ductile-to-brittle transition in spallation of metallic glasses, J. Appl. Phys. **116**, 143503 (2014).

[31] D. Pan, A. Inoue, T. Sakurai, and M. W. Chen, Experimental characterization of shear transformation zones for plastic flow of bulk metallic glasses, Proc. Natl. Acad. Sci. USA **105**, 14769 (2008).

[32] M. L. Manning, J. S. Langer, and J. M. Carlson, Strain localization in a shear transformation zone model for amorphous solids, Phys. Rev. E **76**, 056106 (2007).

[33] J. J. Lewandowski and A. L. Greer, Temperature rise at shear bands in metallic glasses, Nat. Mater. **5**, 15 (2006).

[34] V. Schmidt, H. Rösner, M. Peterlechner, G. Wilde, and P. M. Voyles, Quantitative Measurement of Density in a Shear Band of Metallic Glass Monitored Along its Propagation Direction, Phys. Rev. Lett. **115**, 035501 (2015).

[35] L. Q. Shen, P. Luo, Y. C. Hu, H. Y. Bai, Y. H. Sun, B. A. Sun, Y. H. Liu, and W. H. Wang, Shear-band affected zone revealed by magnetic domains in a ferromagnetic metallic glass, Nat. Commun. **9**, 4414 (2018).

[36] R. Huang, Z. Suo, J. H. Prevost, and W. D. Nix, Inhomogeneous deformation in metallic glasses, J. Mech. Phys. Solids **50**, 1011 (2002).

[37] L. H. Dai, M. Yan, L. F. Liu, and Y. L. Bai, Adiabatic shear banding instability in bulk metallic glasses, Appl. Phys. Lett. **87**, 141916 (2005).

[38] M. Q. Jiang and L. H. Dai, On the origin of shear banding instability in metallic glasses, J. Mech. Phys. Solids **57**, 1267 (2009).

[39] Z. Han, W. Wu, Y. Li, Y. Wei, and H. Gao, An instability index of shear band for plasticity in metallic glasses, Acta Mater. **57**, 1367 (2009).

[40] F. Shimizu, S. Ogata, and J. Li, Yield point of metallic glass, Acta Mater. **54**, 4293 (2006).

[41] A. J. Cao, Y. Q. Cheng, and E. Ma, Structural processes that initiate shear localization in metallic glass, Acta Mater. **57**, 5146 (2009).

[42] Q. K. Li and M. Li, Assessing the critical sizes for shear band formation in metallic glasses from molecular dynamics simulation, Appl. Phys. Lett. **91**, 231905 (2007).

[43] V. Hieronymus-Schmidt, H. Rösner, G. Wilde, and A. Zaccone, Shear banding in metallic glasses described by alignments of Eshelby quadrupoles, Phys. Rev. B **95**, 134111 (2017).

[44] D. Klaumünzer, A. Lazarev, R. Maaß, F. H. Dalla Torre, A. Vinogradov, and J. F. Löffler, Probing Shear-Band

Initiation in Metallic Glasses, Phys. Rev. Lett. **107**, 185502 (2011).

[45] F. Zeng, M. Q. Jiang, and L. H. Dai, Dilatancy induced ductile–brittle transition of shear band in metallic glasses, Proc. R. Soc. A **474**, 20170836 (2018).

[46] C. E. Maloney and A. Lemaître, Amorphous systems in athermal, quasistatic shear, Phys. Rev. E **74**, 016118 (2006).

[47] M. Hassani, A. E. Lagogianni, and F. Varnik, Probing the Degree of Heterogeneity within a Shear Band of a Model Glass, Phys. Rev. Lett. **123**, 195502 (2019).

[48] D. Şopu, A. Stukowski, M. Stoica, and S. Scudino, Atomic-Level Processes of Shear Band Nucleation in Metallic Glasses, Phys. Rev. Lett. **119**, 195503 (2017).

[49] F. Shimizu, S. Ogata, and J. Li, Theory of shear banding in metallic glasses and molecular dynamics calculations, Mater. Trans. **48**, 2923 (2007).

[50] D. Richard, M. Ozawa, S. Patinet, E. Stanifer, B. Shang, S. A. Ridout, B. Xu, G. Zhang, P. K. Morse, J.-L. Barrat, L. Berthier, M. L. Falk, P. Guan, A. J. Liu, K. Martens, S. Sastry, D. Vandembroucq, E. Lerner, and M. L. Manning, Predicting plasticity in disordered solids from structural indicators, Phys. Rev. Materials **4**, 113609 (2020).

[51] G. Zhang, S. A. Ridout, and A. J. Liu, Interplay of Rearrangements, Strain, and Local Structure during Avalanche Propagation, Phys. Rev. X **11**, 041019 (2021).

[52] S. Plimpton, Fast Parallel Algorithms for Short-Range Molecular Dynamics, J. Comput. Phys. **117**, 1 (1995).

[53] Y. Q. Cheng, E. Ma, and H. W. Sheng, Atomic Level Structure in Multicomponent Bulk Metallic Glass, Phys. Rev. Lett. **102**, 245501 (2009).

[54] M. Parrinello and A. Rahman, Polymorphic transitions in single crystals: A new molecular dynamics method, J. Appl. Phys. (Melville, NY) **52**, 7182 (1981).

[55] S. Nosé, A unified formulation of the constant temperature molecular dynamics methods, J. Chem. Phys. **81**, 511 (1984).

[56] W. G. Hoover, Canonical dynamics: Equilibrium phase-space distributions, Phys. Rev. A **31**, 1695 (1985).

[57] H. L. Peng, M. Z. Li, and W. H. Wang, Structural Signature of Plastic Deformation in Metallic Glasses, Phys. Rev. Lett. **106**, 135503 (2011).

[58] E. D. Cubuk, R. J. S. Ivancic, S. S. Schoenholz, D. J. Strickland, A. Basu, Z. S. Davidson, J. Fontaine, J. L. Hor, Y.-R. Huang, Y. Jiang, N. C. Keim, K. D. Koshigan, J. A. Lefever, T. Liu, X.-G. Ma, D. J. Magagnosc, E. Morrow, C. P. Ortiz, J. M. Rieser, A. Shavit *et al.*, Structure-property relationships from universal signatures of plasticity in disordered solids, Science **358**, 1033 (2017).

[59] P. Cao, X. Lin, and H. S. Park, Surface shear-transformation zones in amorphous solids, Phys. Rev. E **90**, 012311 (2014).

[60] P. Cao, M. P. Short, and S. Yip, Understanding the mechanisms of amorphous creep through molecular simulation, Proc. Natl. Acad. Sci. USA **114**, 13631 (2017).

[61] N. Wang, J. Ding, F. Yan, M. Asta, R. O. Ritchie, and L. Li, Spatial correlation of elastic heterogeneity tunes the deformation behavior of metallic glasses, npj Comput. Mater. **4**, 19 (2018).

[62] T. C. Hufnagel, C. A. Schuh, and M. L. Falk, Deformation of metallic glasses: Recent developments in theory, simulations, and experiments, Acta Mater. **109**, 375 (2016).

[63] Z. D. Sha, S. X. Qu, Z. S. Liu, T. J. Wang, and H. Gao, Cyclic deformation in metallic glasses, Nano Lett. **15**, 7010 (2015).

[64] H. Gao, Y. Huang, W. D. Nix, and J. W. Hutchinson, Mechanism-based strain gradient plasticity - I. Theory, J. Mech. Phys. Solids **47**, 1239 (1999).

[65] See Supplemental Material at http://link.aps.org/supplemental/10.1103/PhysRevResearch.4.023220 for further supporting figures.

[66] Z. L. Tian, Y. J. Wang, Y. Chen, and L. H. Dai, Strain gradient drives shear banding in metallic glasses, Phys. Rev. B **96**, 094103 (2017).

[67] L. H. Dai, L. F. Liu, and Y. L. Bai, Formation of adiabatic shear band in metal matrix composites, Int. J. Solids Struct. **41**, 5979 (2004).

[68] X. F. Liu, Z. L. Tian, X. F. Zhang, H. H. Chen, T. W. Liu, Y. Chen, Y. J. Wang, and L. H. Dai, "Self-sharpening" tungsten high-entropy alloy, Acta Mater. **186**, 257 (2020).

[69] N. A. Fleck and J. W. Hutchinson, Strain gradient plasticity, Adv. Appl. Mech. **33**, 295 (1997).

[70] F. Spaepen, Five-fold symmetry in liquids, Nature (London) **408**, 781 (2000).

[71] Y. C. Hu, F. X. Li, M. Z. Li, H. Y. Bai, and W. H. Wang, Five-fold symmetry as indicator of dynamic arrest in metallic glass-forming liquids, Nat. Commun. **6**, 9310 (2015).

[72] M. Zink, K. Samwer, W. L. Johnson, and S. G. Mayr, Plastic deformation of metallic glasses: Size of shear transformation zones from molecular dynamics simulations, Phys. Rev. B **73**, 172203 (2006).

[73] D. Ruan, S. Patinet, and M. L. Falk, Predicting plastic events and quantifying the local yield surface in 3D model glasses, J. Mech. Phys. Solids **158**, 104671 (2022).

[74] A. Ooi, J. Martin, J. Soria, and M. S. Chong, A study of the evolution and characteristics of the invariants of the velocity-gradient tensor in isotropic turbulence, J. Fluid Mech. **381**, 141 (1999).

[75] E. Castillo, *Extreme Value Theory in Engineering* (Academic, New York, 1988).

[76] P. Zhao, J. Li, and Y. Wang, Heterogeneously randomized STZ model of metallic glasses: Softening and extreme value statistics during deformation, Int. J. Plast. **40**, 1 (2013).

[77] P. Cao, M. P. Short, and S. Yip, Potential energy landscape activations governing plastic flows in glass rheology, Proc. Natl. Acad. Sci. USA **116**, 18790 (2019).

[78] D. Stauffer and A. Amnon, *Introduction to Percolation Theory: Revised Second Edition* (Taylor & Francis, London, 1994).

[79] G. P. Shrivastav, P. Chaudhuri, and J. Horbach, Yielding of glass under shear: A directed percolation transition precedes shear-band formation, Phys. Rev. E **94**, 042605 (2016).

[80] P. Cao, K. A. Dahmen, A. Kushima, W. J. Wright, H. S. Park, M. P. Short, and S. Yip, Nanomechanics of slip avalanches in amorphous plasticity, J. Mech. Phys. Solids **114**, 158 (2018).

[81] H. L. Swinney and J. P. Gollub, The transition to turbulence, Phys. Today **31**(8), 41 (1978).

[82] G. Falkovich and K. R. Sreenivasan, Lessons from hydrodynamic turbulence, Phys. Today **59**(4), 43 (2006).